Not accounting for thermokarst ponds leads to overestimation of tundra carbon uptake

Lutz Beckebanze[1,2,*], Zoé Rehder[3,4,*], David Holl[1,2], Charlotta Mirbach[1,2], Christian Wille[5], and Lars Kutzbach[1,2]

[1]Institute of Soil Science, Universität Hamburg, Germany
[2]Center for Earth System Research and Sustainability (CEN), Universität Hamburg, Germany
[3]Department of the Land in the Earth System, Max Planck Institute for Meteorology, Hamburg, Germany
[4]International Max Planck Research School on Earth System Modeling, Hamburg, Germany
[5]Helmholtz-Zentrum Potsdam – Deutsches Geo Forschungs Zentrum (GFZ), Potsdam, Germany
[*]These authors contributed equally to this work.

Correspondence: Lutz Beckebanze (lutz.beckebanze@uni-hamburg.de), Zoé Rehder (zoe.rehder@mpimet.mpg.de)

Abstract. Arctic permafrost landscapes have functioned as a global carbon sink for millennia. These landscapes are very heterogeneous, and the omnipresent water bodies are a carbon source within them. Yet, only a few studies focus on the impact of these water bodies on the landscape carbon budget. We deepen our understanding of carbon emissions from thermokarst ponds and constrain their impact by comparing carbon dioxide and methane fluxes from these ponds to fluxes from the surrounding tundra. We use eddy covariance measurements from a tower located between a large pond and semi-terrestrial tundra.

When taking the open-water areas of thermokarst ponds into account, the carbon dioxide sink strength of the landscape is reduced by 11%. Open-water methane emissions are of similar magnitude as tundra emissions. However, some parts of the pond's shoreline exhibit much higher emissions. This finding underlines the high spatial variability of methane emissions. We conclude that gas fluxes from thermokarst ponds can contribute significantly to the carbon budget of arctic tundra landscapes. Consequently, changes in arctic hydrology and the concomitant changes in the water body distribution may substantially impact the overall carbon budget of the Arctic.

1 Introduction

Water bodies make up a significant part of the arctic lowlands with an areal coverage of about 17% (Muster et al., 2017), and act as an important carbon source in a landscape that is otherwise a carbon sink (Kuhn et al., 2018). Permafrost thaw caused by the warming Arctic will change the distribution of waterbodies (Andresen and Lougheed, 2015; Bring et al., 2016) and thus also their contribution to the landscape-carbon budget (Kuhn et al., 2018). However, data on greenhouse-gas emissions from arctic water bodies are still sparse in space and time, especially data with a high temporal resolution and from non-Yedoma regions (Vonk et al., 2015).

Our study site, in the Lena River Delta, Siberia, is located on an island mostly covered by non-Yedoma polygonal tundra (Fig. 1). This landscape features many ponds, which are defined here by an area $< 8 \cdot 10^4$ m^2, Ramsar Convention Secretariat (2016); Rehder et al. (2021). In our area of interest, ponds cover about as much area as lakes (Abnizova et al., 2012; Muster

et al., 2012). The ponds in this polygonal tundra have formed almost exclusively through thermokarst processes: The ground has a high ice content, so when the ice melts, the ground subsides, and thermokarst ponds form (Ellis et al., 2008). These ponds are often only as big as one polygon, but when several polygons are inundated, larger shallow water bodies form, which we call merged polygonal ponds (Rehder et al., 2021). Ponds emit more greenhouse gases per area than lakes (Holgerson and Raymond, 2016; Wik et al., 2016). Thus, in our study area, they have a higher potential than lakes to counterbalance the carbon sink function of the surrounding tundra (McGuire et al., 2012; Jammet et al., 2017; Kuhn et al., 2018). To better understand the impact of ponds on the landscape carbon flux, we compare carbon dioxide (CO_2) and methane (CH_4) fluxes from the open-water area of ponds to fluxes from the semi-terrestrial tundra, which we define as wet and dry tundra, and overgrown water.

The main driving geophysical and biochemical processes differ between CO_2 and CH_4 emissions. On the one hand, microbial decomposition of dissolved organic carbon, which is introduced laterally into the aquatic system through rain and meltwater (Neff and Asner, 2001), dominates aquatic CO_2 production. When supersaturated with dissolved CO_2, ponds emit CO_2 to the atmosphere through diffusion. While photosynthetic CO_2 uptake has been observed in some clear arctic water bodies (Squires and Lesack, 2003), most arctic water bodies are net CO_2 sources (Kuhn et al., 2018). Estimates range from emissions close to zero (0.028 g m^2 d^{-1} by Treat et al. (2018), or 0.059 g m^2 d^{-1} by Jammet et al. (2017)) to substantial CO_2-C emissions (1.4 – 2.2 g m^2 d^{-1} by Abnizova et al. (2012)).

On the other hand, CH_4 emissions vary even more, sometimes by up to five orders of magnitude within just one site: 0.5 – 6432 mg m^2 d^{-1}, Bouchard et al. (2015). CH_4 is mostly produced in sub-aquatic soils and anoxic bottom waters (Conrad, 1999; Hedderich and Whitman, 2006; Borrel et al., 2011). Additionally, CH_4 can also be produced in the oxic water column (Bogard et al., 2014; Donis et al., 2017), though this pathway only becomes significant in large water bodies (Günthel et al., 2020) and is still under debate (Encinas Fernández et al., 2016; Peeters et al., 2019). Note that during methanogenesis, CO_2 is also formed as a byproduct (Hedderich and Whitman, 2006). CH_4 is then emitted from water bodies through diffusion, ebullition (sudden release of bubbles), and plant-mediated transport. These three pathways lead to high spatial variability between water bodies and within one water body (Sepulveda-Jauregui et al., 2015; Jansen et al., 2019). Especially local seep ebullition causes high spatial variance of CH_4 emissions within one water body when it occurs (Walter et al., 2006). Varying coverage and composition of vascular plants within the shallow parts of a water body can also increase CH_4 variability because each plant species has its specific efficiency in transporting CH_4 (Knoblauch et al., 2015; Andresen et al., 2017).

To study spatial and temporal patterns, we analyze land-atmosphere CO_2 and CH_4 flux observations from an eddy-covariance (EC) tower on Samoylov Island, Lena River Delta, Russia. We set the EC tower up within the polygonal tundra and next to a merged polygonal pond for two months in summer 2019. The polygonal structures are still clearly visible along the shore and underwater, and the pond is mostly shallow (Rehder et al., 2021). Due to the tower's position, fluxes from the merged polygonal pond are the dominant source of the observed EC fluxes under easterly winds. The observed EC fluxes are dominated by semi-terrestrial polygonal tundra with only a low influence from small thermokarst ponds from the other wind directions. We aim to deepen our understanding of carbon emissions from thermokarst ponds and constrain their impact on the landscape carbon

balance. To this end, we (1) compare the water body and tundra fluxes focusing on temporal and spatial patterns, and we (2) investigate the influence of the merged polygonal pond on the landscape carbon balance.

2 Methods

2.1 Study site

Samoylov Island (72°22'N, 126°28'E) lies in the southern part of the Lena River Delta (Fig. 1, b). It has a size of about five km^2 and consists of two geomorphologically different units. The western part ($\sim$2 km^2) is a floodplain annually flooded in spring. The eastern part ($\sim$3 km^2), a late-Holocene river terrace, is characterized by polygonal tundra. The partially degraded polygonal tundra at this study site features a high spatial heterogeneity within a few meters. Dry and wet vegetated parts are interspersed with small and large thermokarst ponds (<1 m^2 – >10000 m^2) and with large thermokarst lakes (up to 0.05 km^2, Boike et al. (2015a); Kartoziia (2019)). The island is surrounded by the Lena River and sandy floodplains, creating more spatial heterogeneity on a larger scale.

We focus on a merged polygonal pond (Fig. 1, d, and A1) in the eastern part of the island. This merged polygonal pond has a size of 0.024 km^2 with a maximum depth of 3.4 meters and a mean depth of 1.2 meters (Rehder et al., 2021; Boike et al., 2015a). On an aerial image, the polygonal structures are still clearly visible under the water surface (Boike et al., 2015c). The vegetated shoreline of this merged polygonal pond is dominated by *Carex aquatilis* interspersed with *Carex chordorrhiza*, *Potentilla palustris* and *Aulacomnium spp.*. These plants grow in the water close to the shore while the deeper parts of the pond are vegetation-free.

2.2 Instruments

We measure gas fluxes using an eddy covariance (EC) tower between July 11 and September 10, 2019. The EC tower is located on the eastern part of Samoylov Island, directly at the western shore of the merged polygonal pond (Fig. 1, d). The EC instruments are mounted on a tripod at the height of 2.25 meters (Fig. A1). The tower is equipped with an enclosed-path CO_2/H_2O sensor (LI-7200, LI-COR Biosciences, USA), an open-path CH_4 sensor (LI-7700, LI-COR Biosciences, USA), and a 3D-ultrasonic anemometer (R3-50, Gill Instruments Limited, UK). All instruments have a sampling rate of 20 Hz. We also install radiation-shielded temperature and humidity sensors at the EC tower (HMP 155, Vaisala, Finland) and use data from a photosynthetically active radiation (PAR) sensor mounted at a tower approximately 500 meters to the west (SKP 215, Skye Instruments, UK). Additional meteorological data for Samoylov Island is provided by Boike et al. (2019).

2.3 Data processing

We perform the raw data processing and computation of half-hourly fluxes for open-path and enclosed-path fluxes using *EddyPro 7.0.6* (LI-COR, 2019). Raw data screening includes spike detection and removal according to Vickers and Mahrt (1997) (1% maximum accepted spikes and a maximum of three consecutive outliners). Additionally, we apply statistical tests

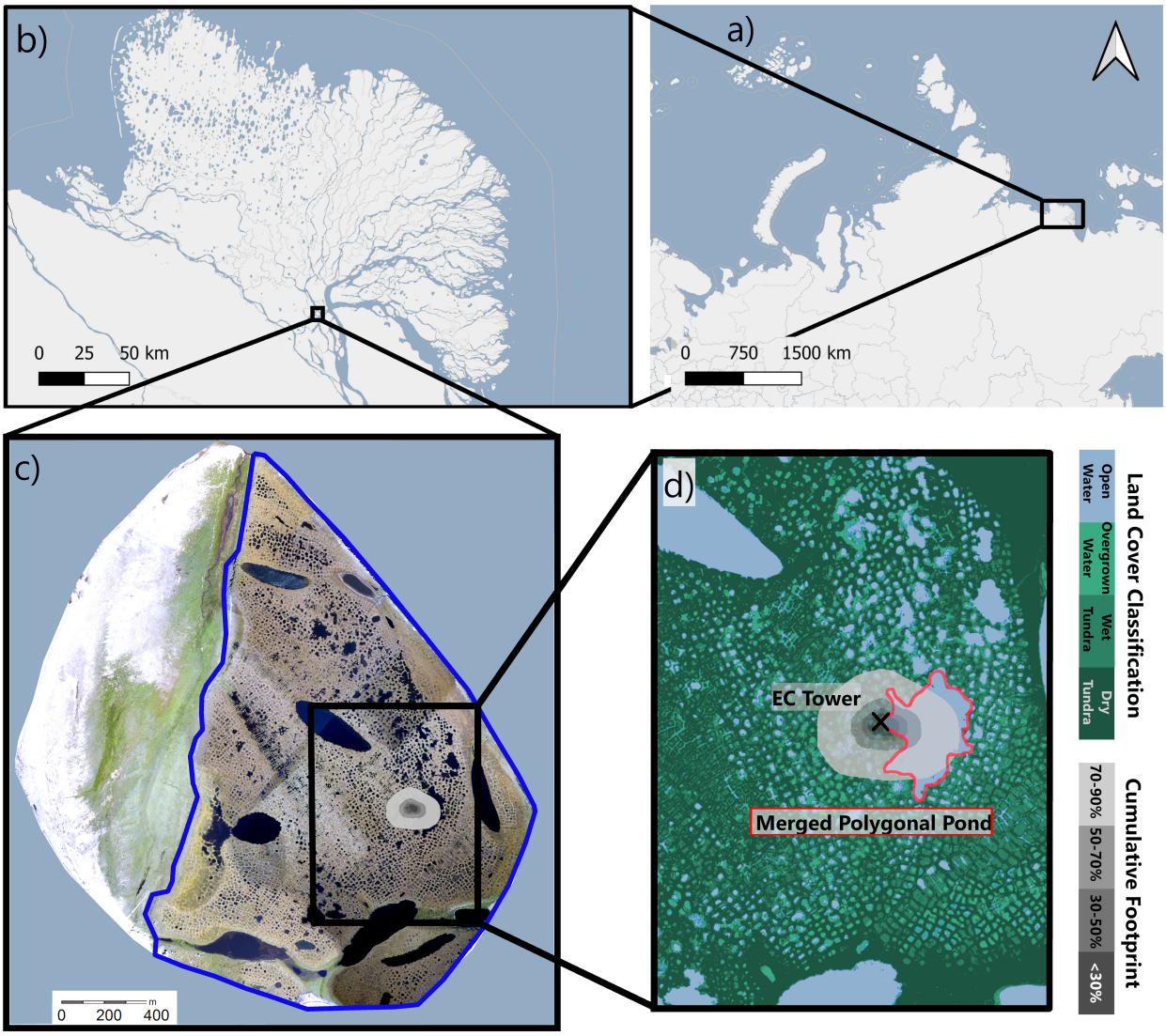

Figure 1. Study site with an overview of Russia (a), the Lena River Delta (b), Samoylov Island with the surrounding Lena River in blue (c), and a close-up look at the study site (d). The EC tower is marked as a black cross with the cumulative footprint (see section 2.4.2) in gray shades surrounding the EC tower. The outline of the land cover classification from section 2.4.1 is shown in a blue line (c). In (d), the detailed land cover classification is shown in blue (open water) and green shades (dark green: dry tundra, medium green: wet tundra, and light green: overgrown water). The merged polygonal pond studied here is outlined in red. Map data from © OpenStreetMap contributors 2020, distributed under the Open Data Commons Open Database License (ODbL) v1.0 (a & b) and modified after Boike et al. (2012) (c & d).

for raw data screening, including tests for amplitude resolution, skewness and kurtosis, discontinuities, angle of attack, and horizontal winds steadiness. All parameters of these tests are set to *EddyPro* default values. We rotate the wind-speed axis to a zero-mean vertical wind speed using the "double rotation"-method by Kaimal and Finnigan (1994). We apply linear detrending following Gash and Culf (1996) to the raw data before flux calculations. We compensate time lags by automatic time-lag optimization using a time-lag-assessment file from a previous EddyPro run. In this previous time-lag assessment, the time lags for all gases are detected by covariance maximization (Fan et al., 1990) resulting in time lags between 0 – 0.4 s for CO_2 and -0.5 – +0.5 s for CH_4. For H_2O, the time lag is humidity-dependent and is calculated for ten humidity classes. We compensate for air-density fluctuations due to thermal expansion/contraction and varying water-vapor concentrations following Webb et al. (1980). This correction depends on accurate measurements of the latent and sensible heat flux and is applied to the open-path data of the LI-7700. Especially for the LI-7700, the correction term can be larger than the flux itself, but the correction is derived from the underlying physical equations. By using *EddyPro*, which uses an up-to-date implementation of the correction, and by using well-calibrated instruments, we are certain to receive accurate CH_4 flux estimations from the LI-7700. For enclosed-path data, we perform a sample-by-sample conversion into mixing ratios to account for air-density fluctuations (Ibrom et al., 2007b; Burba et al., 2012). Flux losses occur in the low- and high-frequency spectral range due to different filtering effects. In the low-frequency range, we compensate flux losses following Moncrieff et al. (2004) and in the high-frequency range following Fratini et al. (2012). For applying the latter method, a spectral assessment file is created using the method by Ibrom et al. (2007a). The spectral assessment results in cut-off frequencies of 3.05 Hz and 1.67 Hz for CO_2 and CH_4, respectively. For H_2O, we find a humidity-dependent cut-off frequency between 1.25 Hz (RH 5 - 45%) and 0.21 Hz (RH 75 - 95%). We perform a quality check on each half-hourly flux following the 0-1-2 system by Mauder and Foken (2004). In this quality check, flux intervals with the lowest quality receive the flag "2" and are excluded from further analysis.

2.4 Data analysis

2.4.1 Land cover classification

The land cover classification covers the late-Holocene river terrace of Samoylov Island. It is based on high-resolution near-infrared (NIR) orthomosaic aerial imagery obtained in the summer of 2008 (Boike et al., 2015b). We use a subset of the existing classification by Muster et al. (2012) as a training dataset to perform a semi-supervised land cover classification using the *maximum likelihood algorithm* in ArcMap Version 10.8 (ESRI Inc, USA). We then apply the ArcMap *majority filter* tool to the new classification. The land cover classification has a resolution of 0.17 m x 0.17 m, it is projected onto WGS 1984 UTM Zone 52N and the classes include *open water*, *overgrown water*, *dry tundra*, and *wet tundra*, as defined by Muster et al. (2012).

2.4.2 Footprint model

The tower location and sensor height are crucial parameters in deploying an EC measurement tower. A lower measurement height results in a smaller footprint. The footprint describes the source area of the flux from the surrounding landscape. With our sensors installed at the height of 2.25 m next to the merged polygonal pond, we expect to observe substantial flux signals

from the adjacent water body as well as from the surrounding polygonal tundra. Each land cover type's contribution to the flux signal depends on the wind direction and turbulence in the atmospheric boundary layer. We implement the analytical footprint model by Kormann and Meixner (2001) in Matlab 2019b (MATLAB, 2019). We combine the footprint model with land cover classification data described in section 2.4.1 to estimate the contribution of each land cover type to each flux signal (from now on referred to as the weighted footprint fraction). The model accounts for the stratification of the atmospheric boundary layer and requires a height-independent crosswind distribution and horizontal homogeneity of the surface. The input data requires stationarity of atmospheric conditions during the flux intervals of 30 minutes. We derive the vertical power-law profiles for the eddy diffusivity and the wind speed for each 30-minute flux depending on the atmospheric stratification (equation 6 in Kormann and Meixner (2001)). We use an analytical approach to find the closest Monin-Obukhov (M-O) similarity profile (equation 36 in Kormann and Meixner (2001)). Next, we calculate a two-dimensional probability density function of the source area for each flux (from equations 9 and 21 in Kormann and Meixner (2001)). We combine each probability density function with the land cover classification of the river terrace of Samoylov Island, with its four land cover types (see section 2.4.1). The resolution of the footprint model is set to the land cover classification resolution of 0.17 m x 0.17 m. Hence, we can estimate how much a given grid cell contributes to each 30-min flux. We also know each grid cell's dominant land cover type from the land cover classification. We combine both information for each grid cell and calculate the sum of the fraction fluxes within the source area for each of the four land-cover types (*dry tundra*, *wet tundra*, *overgrown water*, and *open water*) and obtain the contribution of each land cover type to each 30-minute flux ($a_{dry\ tundra}$, $a_{wet\ tundra}$, $a_{overgrown\ water}$, and $a_{open\ water}$). We refer to this contribution of each land cover type as the *weighted footprint fraction*.

We also sum all 30-min two-dimensional probability density functions over the whole deployment time. This sum is referred to as the cumulative footprint (gray shaded area in Fig. 1, c–d). The light gray area's outer boundary represents the 90% isoline, and the light gray area's inner boundary is the 70% isoline of the cumulative footprint. The 90% isoline means that it is likely that 10% of each observed flux signal originates from outside of the light gray area. Medium gray represents 50-70%, medium-dark gray 30-50%, and dark gray indicates a probability of less than 30% that each observed flux signal originates from within the marked area.

2.4.3 Gap-filling the CO_2 flux

To gap-fill the net-ecosystem exchange (NEE) fluxes of CO_2, we use the *bulk-NEE model* by Runkle et al. (2013). The model uses the total ecosystem respiration (TER) and the gross primary production (GPP) to gap-fill NEE, our target variable. The model is specifically designed to model NEE in arctic regions: It takes impacts of the polar day into account. We estimate all model parameters for running 5-day periods to capture changing plant physiology during the measurement period.
NEE is partitioned into two components (equation 3): TER (µmol m^{-2} s^{-1}, equation 1) and GPP (µmol m^{-2} s^{-1}, equation 2). Parameters of both components are fit simultaneously. TER is modeled as an exponential function of air temperature T_{air}:

$$\mathrm{TER} = R_{base} \cdot Q_{10}^{\frac{T_{air}-T_{ref}}{\gamma}} \tag{1}$$

where $T_{ref} = 15$ °C and $\gamma = 10$ °C are constant, independent parameters. R_{base} (µmol m^{-2} s^{-1}) describes the basal respiration at the reference temperature T_{ref} and Q_{10} (dimensionless) the sensitivity of ecosystem respiration to air temperature changes.

GPP is modeled as a rectangular hyperbolic function of PAR (µmol m^{-2} s^{-1}):

$$\mathrm{GPP} = -\frac{P_{max} \cdot \alpha \cdot \mathrm{PAR}}{P_{max} + \alpha \cdot \mathrm{PAR}} \tag{2}$$

where α (µmol μmol^{-1}) is the initial canopy quantum use efficiency (slope of the fitted curve at PAR= 0) and P_{max} (µmol m^{-2} s^{-1}) the maximum canopy photosynthetic potential for PAR $\rightarrow \infty$.

We sum both components to estimate the modeled NEE $F_{CO_2,mod}$:

$$F_{CO_2,mod} = \mathrm{TER} + \mathrm{GPP}. \tag{3}$$

We split the datasets into a training (70%) and a validation (30%) data set to test model performance. In 38 5-day fitting periods, we find an R^2 above 0.9 between the model output and the validation set. Eighteen times, we get an R^2 between 0.8 – 0.9 and six times an R^2 below 0.7. The model performance indicates that the model works well overall. In the model input, we exclude CO_2 fluxes with an absolute value of more than 4 g m^{-2} d^{-1}. We additionally exclude CO_2 fluxes from the wind direction (WD) of the merged polygonal pond (30°< WD <150°) from the training dataset to obtain a dataset consisting of as much semi-terrestrial tundra as possible. We perform this step since we expect little to no photosynthetic activity in the open-water part of the merged polygonal pond.

We implement the *bulk model* in Matlab 2019b (MATLAB, 2019) using the *fit* function with the fitting method of *NonLinearLeastSquares*. We use the *coeffvalues*-function to estimate the four parameters and the *confint*-function to estimate their 95% confidence bounds. All partitioned fluxes are converted into CO_2-C fluxes in the unit g m^{-2} d^{-1} before the data analysis.

2.4.4 The open-water CO_2 flux

We want to extract fluxes from ponds and semi-terrestrial tundra to analyze the influence of ponds on a polygonal tundra landscape. However, due to the strong heterogeneity of the landscape and the relatively small size of the merged polygonal pond compared to the EC footprint, we measure a mixed signal from all wind directions. In other words, each flux measured with the EC method contains information from different land cover types. Since we are interested in average tundra fluxes, we combine the landcover classes dry tundra, wet tundra, and overgrown water under the term *semi-terrestrial tundra*. In this way, we can compare two landcover classes, semi-terrestrial tundra and the open water from thermokarst ponds.

Similar approaches of analyzing heterogeneous eddy covariance fluxes in arctic environments have been conducted for CO_2 and CH_4 (e.g. Rößger et al., 2019a,b; Tuovinen et al., 2019). Rößger et al. (2019a,b) extracted CO_2 and CH_4 fluxes from two different land cover classes on a floodplain, and Tuovinen et al. (2019) separated CH_4 fluxes from nine individual land cover classes, including water, and combined them into four source classes (no separate class for water). All three studies have in common that they differentiate fluxes from different vegetation types. However, our method is dedicated to distinguishing between fluxes from tundra and water.

To estimate the CO_2 flux from the merged polygonal pond (F_{pond}), we first fit the *bulk model* to data excluding fluxes from the direction of the merged polygonal pond (thus exclude fluxes from 30°< WD <150°, as described in section 2.4.3). With this bulk model, we gap-fill the CO_2 flux, and the gap-filled CO_2 flux ($F_{modeled,mix}$) represents the semi-terrestrial tundra surrounding the EC tower, including small ponds to the north, west, and south. Second, we assume that the total observed flux is a linear combination of the fluxes from the land cover types weighted by their respective contribution to the footprint. Thus, we postulate that the observed CO_2 flux ($F_{obs,mix}$, not gap-filled) is the sum of the individual land cover type fluxes ($F_{modeled,mix}$ and the merged polygonal pond F_{pond}) each multiplied with their weighted footprint fraction (a_{tundra} and a_{pond}), with $a_{open\ water} = a_{pond}$, $a_{tundra} = a_{sum} - a_{pond}$, and a_{sum} is the sum over all land cover classes:

$$\begin{aligned} F_{obs,mix} &= a_{pond} \cdot F_{pond} + a_{tundra} \cdot F_{modeled,mix} \\ \Leftrightarrow F_{pond} &= \frac{F_{obs,mix} - a_{tundra} \cdot F_{modeled,mix}}{a_{pond}} \end{aligned} \quad (4)$$

To improve data quality, we exclude 30-min fluxes of F_{pond} when $a_{pond} < 50\%$. Then, we use the median of F_{pond} for further calculations, and we assume that all open water in the EC footprint emits the same amount of CO_2.

As mentioned above, the observed CO_2 flux from the north, west, and south ($F_{obs,mix}$) is still influenced by small thermokarst ponds. To analyze in detail the CO_2 flux from the semi-terrestrial tundra ($F_{modeled,tundra}$), we subtract the previously estimated pond-CO_2 flux F_{pond} from the observed CO_2 flux $F_{obs,mix}$:

$$F_{modeled,tundra} = \frac{F_{obs,mix} - a_{pond} \cdot F_{pond}}{a_{tundra}} \quad (5)$$

We then use this estimated CO_2 flux from the semi-terrestrial tundra $F_{modeled,tundra}$ as the input variable for the *bulk model* to receive a gap-filled dataset of CO_2 flux from semi-terrestrial tundra.

To evaluate the impact of ponds on the landscape CO_2 flux, we estimate a polygonal-tundra landscape-CO_2 flux ($F_{landscape}$) by linearly combining ponds and semi-terrestrial tundra:

$$F_{landscape} = A_{pond} \cdot F_{pond} + A_{tundra} \cdot F_{modeled,tundra}$$

where F_{pond} describes the CO_2 emission from the open-water areas of ponds (equation 4), $F_{modeled,tundra}$ the modeled CO_2 flux from the semi-terrestrial tundra (equation 5), $A_{pond} = 0.07$ the coverage of open pond water on the whole river terrace of Samoylov Island (from the land cover classification, section 2.4.1) and $A_{tundra} = 1 - 0.07$ the coverage of other land cover types. We do not account for (larger, deeper) thermokarst lakes in this up-scaling approach, as we expect different greenhouse gas emissions from these lakes and there are no lakes in our footprint. Thus, we scale the above numbers to $A_{tundra} + A_{pond} = 1$ which results in $A_{pond} = 0.076$ and $A_{tundra} = 0.924$.

2.4.5 CH_4 flux partitioning

Since we do not have a simple gap-filling model at hand for CH_4 emissions from the tundra, and since CH_4 emissions are much more variable than CO_2 emissions, we treat CH_4 differently. We focus on wind sectors instead of extracting the fluxes from the landcover types. We divide fluxes into the following wind sectors:

- *tundra*: At least half of the footprint consists of dry tundra, and the wind direction is larger than 170°.
- $shore_{50°}$: Less than 40% of the footprint consists of dry tundra and water contributed to the footprint with at least 30%. The wind direction lies between 30°< WD <65°.
- *pond*: At least half of the footprint consists of open water, and the wind direction lies between 65°< WD <110°.
- $shore_{120°}$: Less than 40% of the footprint consists of dry tundra and water contributed to the footprint with at least 30%. The wind direction lies between 110°< WD <130°.

2.4.6 CH_4 permutation test

To evaluate whether the differences in medians between the four wind sectors are significant, we apply a permutation test (Edgington and Onghena, 2007). In this test, we randomly assign each 30-min flux to one of two groups and calculate both groups' median and their differences. Using the four wind sectors, we do six tests in total. After repeating this step 10000 times, we plot the resulting differences in medians in a histogram and perform a one-sample t-test to evaluate whether the observed difference in medians differs significantly ($p<0.01$) from the randomly generated differences.

3 Results

3.1 Meteorological conditions

During the measurement period between 11 July and 10 September 2019, half-hourly air temperatures range from -0.5 °C to 27.6 °C with a mean temperature of 8.7 °C (Fig. A2, a). The maximum wind speed measured on the EC tower at 2.25 m height is 8.9 m s^{-1} (Fig. A2, b). Photosynthetically active radiation (PAR) reaches values of up to 1419 µmol m^{-2} s^{-1} with decreasing maximum values during the measurement period (Fig. A2, c). 28 cloudy days are visible as days with low PAR-values (below ∼500 µmol m^{-2} s^{-1}) throughout the measurement period.

3.2 CO_2 fluxes

When inspecting the relation between observed CO_2 fluxes and wind direction (Fig. 2), we find that the CO_2 flux exhibits a high temporal variability between positive and negative CO_2 fluxes from most wind directions. In the wind sector between 60° – 120°, the flux is dominated by the merged polygonal pond. The CO_2-C fluxes from this pond sector show a smaller variability (mean of 0.06 g m^{-2} d^{-1} with a standard deviation of 0.28 g m^{-2} d^{-1}) than the fluxes from all other wind directions (mean of -0.17 g m^{-2} d^{-1} with a standard deviation of 0.77 g m^{-2} d^{-1}). Additionally, we observe a lower respiration rate from the pond than from the semi-terrestrial tundra. Fig. 3 shows the observed night-time CO_2 fluxes plotted against the respective weighted footprint fraction of open water. We define nighttime as PAR<20 µmol m^{-2} s^{-1} and expect only respiration and no photosynthesis during these times. We find that the fluxes decrease with an increasing open-water contribution. Thus, the strength of respiration shows a dependence on the open-water contribution. We also find that low air temperatures are mostly associated with low respiration rates.

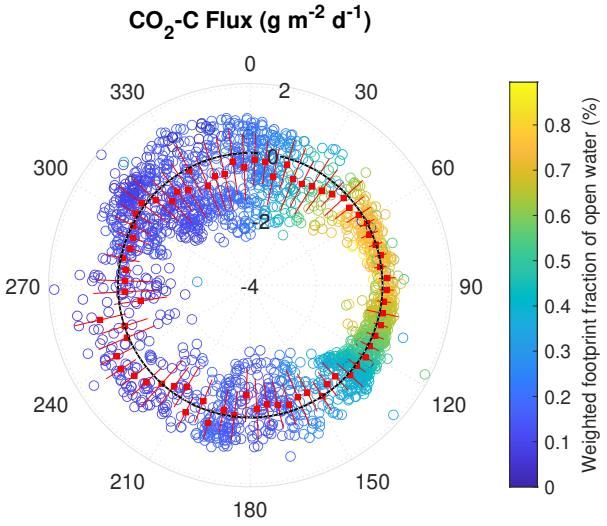

Figure 2. Polar plot of observed 30-min CO_2-C flux with respect to the wind direction at the EC tower. Negative values (inside of the dotted black line) represent CO_2 uptake, positive values (outside of the dotted black line) CO_2 emission. The values -4, -2, 0, and 2 indicate the magnitude of the CO_2-C flux in g m^{-2} d^{-1}. The color represents the percentage of open water weighted footprint fraction in each 30-minute flux. The red boxes indicate the mean CO_2 flux of 5° wind direction intervals during the 2-months observation period (red lines indicate the first standard deviation).

Another part of the CO_2 variability stems from the diurnal cycle. We compare the diurnal cycle of the CO_2 fluxes from the merged polygonal pond (estimated following equation 4) and the semi-terrestrial tundra (Eq. 5, Fig. 4), and we see a less pronounced diurnal CO_2 cycle from the direction of the merged polygonal pond (blue) compared to the diurnal CO_2 cycle from the tundra (green). All data from the merged polygonal pond combined (F_{pond} in Eq. 4) result in a CO_2-C flux of $\mathbf{0.13}\ ^{\mathbf{0.24}}_{\mathbf{0.00}}$ g m^{-2} d^{-1} (Median $^{75\%\ \text{Percentile}}_{25\%\ \text{Percentile}}$).

3.3 CH_4 fluxes

When plotting observed CH_4 fluxes against wind direction (Fig. 5), we see that the CH_4 emissions peak at $\sim 120°$, where fluxes from one shoreline of the merged polygonal pond contribute to the observed flux (Fig. 1 d, from now on $shore_{120°}$). We do not observe a similar peak of CH_4 emissions in the direction of the second shoreline towards $\sim 50°$ ($shore_{50°}$). These peaks did not correlate with any of the four land-cover classes.

To further investigate the peak at $shore_{120°}$, we compare the CH_4 emissions from the different wind sectors ($shore_{120°}$, $shore_{50°}$, *pond* and *tundra*, section 2.4.5). We find the following fluxes from the wind sectors: 19.18 $^{24.47}_{14.26}$ mg m^{-2} d^{-1} ($shore_{120°}$), 12.96 $^{15.11}_{10.34}$ mg m^{-2} d^{-1} ($shore_{50°}$), 13.90 $^{18.46}_{11.02}$ mg m^{-2} d^{-1} (*pond*), and 12.55 $^{16.07}_{9.65}$ mg m^{-2} d^{-1} (*tundra*, $Median\ ^{75\%Percentile}_{25\%Percentile}$). Fluxes from $shore_{120°}$ have a higher median than fluxes from the other three wind sectors (Fig. 6).

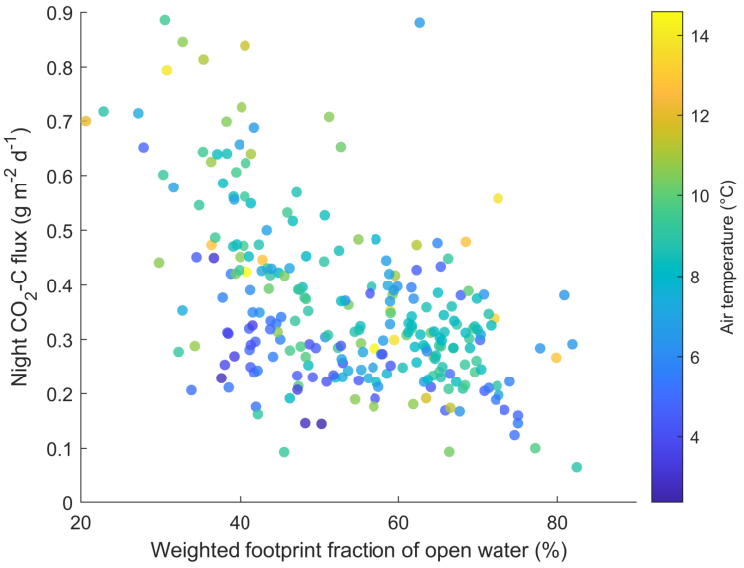

Figure 3. Scatter plot of observed CO_2 fluxes against the weighted footprint fraction of open water in each 30-minute flux with temperature as color. Only fluxes at nighttime (PAR<20 µmol m^{-2} s^{-1}) are shown.

We investigated the impact of wind and air temperature on the CH_4 fluxes by excluding flux intervals with high wind speed (larger than 5 m s^{-1}) and high air temperature (larger than 12 °C). In the randomization test (section 2.4.6), we find evidence for a significant difference between the CH_4 emission from $shore_{120^\circ}$ and the other three classes at low wind speeds (top row in Fig. A4) and no significant difference between the CH_4 emission from the classes *pond* - *tundra* and $shore_{50^\circ}$ - *tundra*. The difference between the classes *pond* and $shore_{50^\circ}$ is significant, however much smaller than the previously described differences (center graph in Fig. A4). Note that the CH_4 emissions from the pond and the tundra have a similar magnitude under moderate wind speed conditions. The results are very similar for moderate temperatures: We find evidence for a significant difference between the CH_4 emission from $shore_{120^\circ}$ to the other three classes (top row in Fig. A5). The differences in medians between the *pond* and $shore_{50^\circ}$ and between the *pond* and *tundra* are significant. However, this difference is much smaller (second row in Fig. A5). In summary, we find that neither high wind speed nor high temperatures act as a driver for the high CH_4 emission from $shore_{120^\circ}$.

The ratio of CO_2-C to CH_4-C emissions at night (PAR<20 µmol m^{-2} s^{-1}) has a value of $CH_4/CO_2 = 0.060^{0.076}_{0.049}$ for fluxes with an open-water weighted footprint fraction of more than 60%, whereas the ratio amounts to ($CH_4/CO_2 = 0.020^{0.024}_{0.015}$, $\text{Median}^{75\%\text{ Percentile}}_{25\%\text{ Percentile}}$) for fluxes with an open-water weighted footprint fraction of less than 20%.

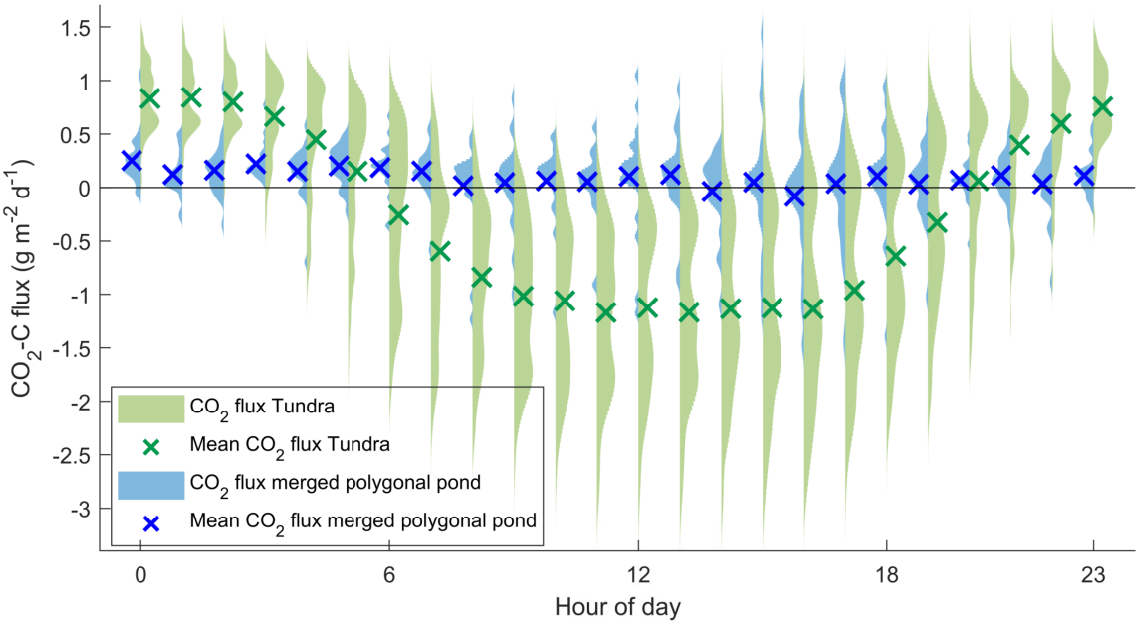

Figure 4. Diurnal cycle of modeled CO_2-C flux from the merged polygonal pond (blue, eq. 4) and the tundra (green, eq. 5) as violin plots for each half-hour flux. Blue and green crosses mark the mean CO_2-C flux during each half-hour flux. A violin plot shows the distribution of measurements along the y-axis – the width of the curves expresses the density of data points at each y-value.

3.4 Upscaled CO_2 flux

We use the estimated open-water CO_2 flux from the merged polygonal pond and the modeled CO_2 flux from the semi-terrestrial tundra to linearly up-scale the CO_2 flux for the polygonal tundra of Samoylov Island (excluding larger thermokarst lakes, the method described in section 2.4.4). As we have no estimates for the CH_4 fluxes from the landcover types *tundra* and *pond*, we only upscale CO_2.

We estimate that the landscape CO_2 uptake is $\sim 11\%$ lower when including the CO_2 flux from ponds compared to a semi-terrestrial tundra without ponds. The modeled CO_2-C flux from the semi-terrestrial tundra (without consideration of pond fluxes) accumulated to -16.29 $\pm$ 0.43 g m^{-2} during the observation period (60.5 days). Separated into months, it amounts to -15.01 $\pm$ 0.26, -3.56 $\pm$ 0.33 and +2.35 $\pm$ 0.11 g m^{-2} in July (19.8 days), August (31 days), and September (9.7 days), respectively. When including the CO_2 flux from the merged polygonal pond as representative for all ponds on Samoylov island, the resulting estimate of the landscape CO_2 flux amounts to -14.47 $\pm$ 0.40 g m^{-2} (60.5 days) and monthly fluxes of -13.75 $\pm$ 0.24, -2.99 $\pm$ 0.31, and +2.27 $\pm$ 0.10 g m^{-2} in July (19.8 days), August (31 days), and September (9.7 days), respectively. Thus, ponds have the largest impact on the landscape CO_2 flux in August. In September, accounting for ponds leads to 3.5% lower landscape emissions.

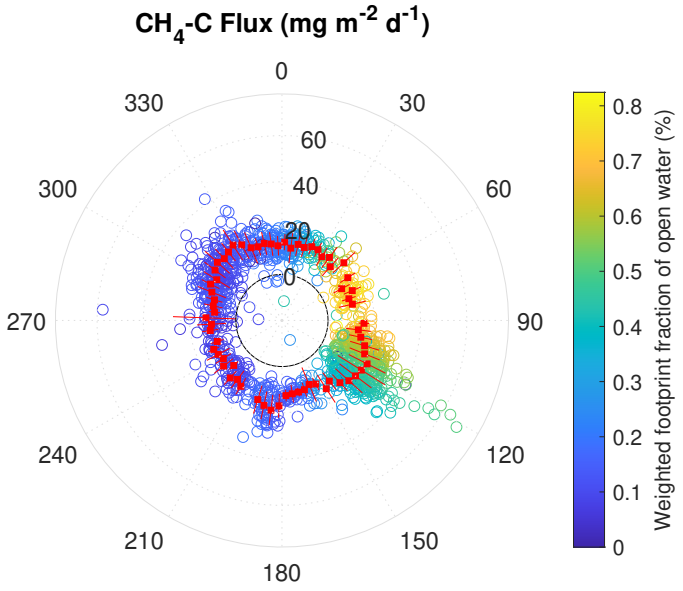

Figure 5. Polar plot of 30-minute observed CH_4-C flux with respect to the wind direction at the EC tower. Positive values outside the dotted black line represent CH_4 emission, and inside the line, CH_4 uptake during one half-hour period. The values 0, 20, 40, and 60 indicate the magnitude of the CH_4-C flux in mg m^{-2} d^{-1}. The color represents the percentage of open water weighted footprint fraction in each flux. The red boxes indicate the mean CH_4 flux of 5° wind direction intervals during the 2-months observation period (red lines indicate the first standard deviation).

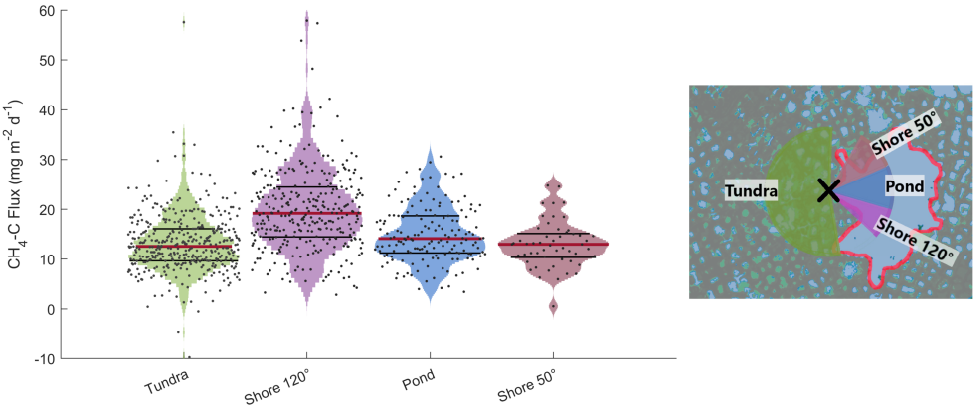

Figure 6. Violin plots of observed CH_4 emissions at the EC tower separated into four different wind direction classes. A violin plot shows the distribution of measurements along the y-axis - the width of the curves expresses the density of data points at each y-value. Medians of CH_4 emission distributions are shown as red lines, and 75^{th} & 25^{th} percentile are shown as black lines. On the right, the wind sectors with the eddy covariance tower in the center (black cross) are shown.

4 Discussion

4.1 CO_2 flux

Only a limited number of EC CO_2-flux studies from permafrost-affected ponds and lakes are available (studies with "EC" in Tab. 1). Estimates of open-water EC CO_2-C flux range from 0.059 g m^{-2} d^{-1} (Jammet et al., 2017) over 0.11 g m^{-2} d^{-1} (Eugster et al., 2003) to 0.22 g m^{-2} d^{-1} (Jonsson et al., 2008). Our estimate of $0.12\,^{0.24}_{0.0014}$ g m^{-2} d^{-1} is, therefore, well within the range of open-water CO_2-C fluxes observed with the EC method. Other studies using different methods report a wider range of open-water CO_2 fluxes in arctic regions. These fluxes range from a CO_2-C uptake (-0.14 g m^{-2} d^{-1}, Bouchard et al. (2015)) to substantial emissions of CO_2-C (up to 2.2 g m^{-2} d^{-1}, Abnizova et al. (2012)). A modeling study involving multiple lakes in north-eastern European Russia found close to zero emissions (0.028 g m^{-2} d^{-1}, Treat et al. (2018)). Our perhaps most striking finding is that our estimates of open-water CO_2 emissions are approx. 12-18 times smaller than previously reported for open-water CO_2 emissions at the same study site (Abnizova et al., 2012). One reason for the divergent results might be the different methods used. In Abnizova et al. (2012), the thin boundary layer model (TBL) after Liss and Slater (1974) was applied to estimate CO_2 emissions from CO_2 concentrations measured in water samples. However, one other study found good agreement between the EC method and the TBL (Eugster et al., 2003). Abnizova et al. (2012) measured smaller thermokarst ponds, as opposed to the larger merged polygonal pond we focus on. While this might explain the deviations, there are also thermokarst ponds highly similar to the ones in Abnizova et al. (2012) in the footprint of the EC tower in this study. If those ponds emitted CO_2 in the quantities suggested by Abnizova et al. (2012), we would expect to see their signal more clearly in our measurements. Thus, we cannot conclusively resolve the differences.

Our approach of combining a footprint model with a land-cover classification to extract fluxes from different land-cover classes allows us to determine the pond CO_2 flux. We report an uncertainty range of the pond CO_2 flux; however, we cannot identify the full uncertainty of this flux in this approach due to the unknown uncertainty of the footprint analysis. Still, the pond CO_2 flux results are plausible and in the correct order of magnitude for two reasons. First, a reduced diurnal variability has been observed when the pond influences the flux signal (Fig. 4). This reduction indicates that the respiration rate from the pond is lower than the respiration rate from the semi-terrestrial tundra, where ample oxygen is available in the upper soil layer. Additionally, there is less photosynthesis since the ponds have a lower vegetation density than the tundra. Second, when focusing on night-time fluxes, when only respiration occurs, and no carbon is taken up, there is a decrease in CO_2 emission with an increasing weighted footprint fraction of open water (Fig. 3), also indicating reduced decomposition in the pond. Overall, the lower emissions from the pond compared to the semi-terrestrial tundra are reasonable.

4.2 CH_4 flux

We observe large differences in CH_4 emission from different wind sectors. CH_4 emissions from $shore_{120^\circ}$ are significantly higher than from $shore_{50^\circ}$, *pond* or *tundra* (section 3.3). Notably, we tested the dependence of these higher fluxes on wind speed and air temperature. We expect high wind speeds to enhance turbulent mixing of the water column and diffusive CH_4 outgassing at the water-atmosphere interface. High wind speeds are also associated with pressure pumping, which potentially

Table 1. Daily mean water-atmosphere CO_2 & CH_4 fluxes from different study sites. TBL is the abbreviation for thin boundary layer model, EC for eddy covariance, CH for chamber measurement, MOD for modelled fluxes, STO for storage fluxes, and NEW for the method used in this study. All fluxes are given ± standard deviation, except of fluxes from this study are given as Median $^{75\%\ \text{Percentile}}_{25\%\ \text{Percentile}}$.

Study	Location	Period/Time	Study Site	Method	CO_2-C flux ($g\ m^{-2}\ d^{-1}$)	CH_4-C flux ($mg\ m^{-2}\ d^{-1}$)
This study	Lena Delta, Northern Siberia	11.07.– 10.09.2019	merged polygonal pond	EC/NEW	$0.13\ ^{0.24}_{0.00}$	$14.10\ ^{18.67}_{11.23}$
			merged polygonal pond shore	EC	–	$12.96\ ^{15.11}_{10.34} - 19.18\ ^{24.47}_{14.26}$
Abnizova et al. (2012)	Lena Delta, Northern Siberia	01.08. – 21.09.2008	Samoylov Pond	TBL	1.50 – 2.20	–
			Samoylov Lake	TBL	1.40 – 2.10	–
Jammet et al. (2017)	Northern Sweden	2012 – 2013	Lake Villasjön	EC	0.059	13.42 ± 1.64
Jonsson et al. (2008)	Northern Sweden	17.06. – 15.10.2005	Lake Merasjärvi	EC	0.22 ± 0.002	–
				TBL	0.30 ± 0.01	
Eugster et al. (2003)	Alaska	27.07 – 31.07.1995	Toolik Lake	EC	0.11 ± 0.033	–
				TBL	0.13 ± 0.003	
				CH	0.37 ± 0.060	
Jansen et al. (2019)	Northern Sweden	Year round, 2010 – 2017	Villasjön	CH	0.22 ± 0.047	14.04 ± 2.25
			Inre Harrsjön		0.25 ± 0.05	10.39 ± 1.40
			Mellersta Harrsjön		0.73 ± 0.067	13.76 ± 2.81
Bouchard et al. (2015)	NE Canada	July 2013 & 2014	Bylot Island, Polygon ponds	TBL	-0.14 – 0.74	0.50 – 6432
			Lakes		-0.085 – 0.062	0.70 – 74.5
Sepulveda-Jauregui et al. (2015)	Alaska	June – July 2011 & 2012	8 Lakes, Yedoma	TBL & STO	0.60 ± 0.58	92.86 ± 35.72
			32 Lakes, Non-Yedoma		0.10 ± 0.10	16.80 ± 8.61
Treat et al. (2018)	Northeast European Russia	2006 – 2015	Multiple Lakes	MOD	0.028 ± 0.00011	0.84 ± 0.0
Sieczko et al. (2020)	Northern Sweden	July – August 2017	Lake Ljusvatterntjärn	CH	–	2.95 ± 0.75
Ducharme-Riel et al. (2015)	North-East Canada	Summer 2008	15 lakes	TBL	0.20 ± 0.093	–
Repo et al. (2007)	Western Siberia	03.07. – 06.09.2005	MTlake	TBL	0.14 ± 0.11	–
			FTlake	TBL	0.41 ± 0.25	
			MTpond	TBL	0.44 ± 0.25	
Lundin et al. (2013)	Northern Sweden	2009 (only ice-free season)	27 lakes	TBL	0.18 ± 0.11	–
Kling et al. (1992)	Alaska	1975 – 1989	25 lakes	TBL	0.25 ± 0.040	5.16 ± 0.96

fosters the ebullition of CH_4. On the other hand, peak temperatures can lead to peak CH_4 production and emissions due to enhanced biological activity. However, the high emissions from $shore_{120^\circ}$ do not coincide with meteorological conditions of high wind speeds or high temperatures, which would especially favor high emissions. Thus, the difference between $shore_{120^\circ}$ and $shore_{50^\circ}$ is astounding since the shorelines share many characteristics. Both extend radially (in a straight line) from the EC tower (Fig. 1), thus contributing similarly to the EC flux. The underwater topography does not vary much between the two shorelines. Both shorelines have a water depth between a few centimeters and a few decimeters within meters away from the shore (see data from Boike et al. (2015a)). As previously described in section 2.1, both shorelines are dominated by *Carex aquatilis*, and from visual inspection, we cannot find differences in shoot density. We, therefore, assume that the vegetation type does not play a major role in explaining the differences between the CH_4 emission from $shore_{120^\circ}$ and $shore_{50^\circ}$. We also examine the evolution of the shorelines at the merged polygonal pond to check whether erosion along the shoreline could drive the high CH_4 emissions. We compare a coarse image from 1965 (U.S. Geological Survey, EROS Center, 1965) with the current shoreline, yet we cannot identify signs of recent erosion. Also, high-resolution aerial images of the pond from 2008 (Boike et al. (2015b), resolution > 0.33 m) and 2015 (Boike et al. (2015c), resolution > 0.33 m) show no signs of erosion. Thus, we exclude erosion as a driving factor of high CH_4 emissions.

We also consider the possibility that local ebullition of the pond could lead to high CH_4 emissions from $shore_{120^\circ}$. We apply the method proposed by Iwata et al. (2018) to check for signs of ebullition events. This method uses the 20 Hz raw concentration of CH_4 to detect short-term peaks in CH_4 that originate from ebullition events. However, we cannot detect ebullition events in the 20 Hz raw data.

In summary, many causes, such as meteorological conditions (wind speed or temperature), vegetation type, coastal erosion, and intense ebullition events, can be excluded as driving factors. Therefore, the most likely cause of the higher CH_4 emissions from $shore_{120^\circ}$ might be a small but steady seep ebullition hot spot close to this shoreline (such as ebullition class *Kotenok* in Walter et al. (2006)). Seep ebullition hot spots have been reported to occur heterogeneously in clusters in Alaskan lakes (Walter Anthony and Anthony, 2013). So, a future visual inspection of trapped CH_4 bubbles in the ice column during wintertime, as proposed in Vonk et al. (2015), could reveal more information about the cause of the higher CH_4 emission from the $shore_{120^\circ}$, as could funnel or chamber measurements with high spatial coverage.

The merged polygonal pond emits CH_4 with a similar magnitude as the tundra surface under similar meteorological conditions and when excluding the high emissions from $shore_{120^\circ}$. However, substrate availability and temperature dynamics differ substantially. Additionally, in dense soils, methane diffuses through upper soil layers and can oxidize before reaching the surface. In contrast, methane emitted in ponds can reach the surface quickly through ebullition or higher plant-mediated transport in addition to diffusion. Therefore, we expect bigger differences between CH_4 emissions from the pond and the tundra, more like the differences detected in a subarctic lake and fen (Jammet et al., 2017). Yet, we see no significant difference in CH_4 emission from the open-water areas of the merged polygonal pond and the tundra surface (Fig. 6 & A4).

Since many other ponds are smaller than the pond (making them unsuitable for studying with the EC method), and since smaller ponds tend to be stronger emitters (Holgerson and Raymond, 2016; Wik et al., 2016), our measurements might provide a lower limit of overall pond-CH_4 emissions.

We estimate a CH_4-C flux of 13.38 $^{15.92}_{10.55}$ mg m^{-2} d^{-1} ($Median$ $^{75\%Percentile}_{25\%Percentile}$) from the merged polygonal pond and 12.96 $^{15.11}_{10.34}$ – 19.18 $^{24.47}_{14.26}$ mg m^{-2} d^{-1} from the shores of this pond. This is higher than the fluxes measured by Jammet et al. (2017) from a sub-arctic lake (Tab. 1). The authors report a mean annual CH_4-C flux of 13.42 $\pm$ 1.64 mg m^{-2} d^{-1} and a mean ice-free season CH_4-C flux of 7.58 $\pm$ 0.69 mg m^{-2} d^{-1}. A study focusing on 32 non-Yedoma thermokarst lakes in Alaska found CH_4-C emissions similar to our results (16.80 $\pm$ 8.61 mg m^{-2} d^{-1}, Sepulveda-Jauregui et al. (2015)). Also, a synthesis of 149 thermokarst water bodies north of $\sim 50^{\circ}$ reports CH_4-C emissions in the same order of magnitude (27.57 $\pm$ 14.77 mg m^{-2} d^{-1}, Wik et al. (2016)). However, there is also a recent study reporting considerably lower CH_4-C emissions of 2.95 $\pm$ 0.75 mg m^{-2} d^{-1} in Northern Sweden (Sieczko et al., 2020) and, in contrast, a study finding CH_4-C emissions of up to 6432 mg m^{-2} d^{-1} in North-East Canada (Bouchard et al., 2015). The wide range of water-body methane emissions cautions us to be careful when generalizing our results even for Samoylov Island, especially since the emissions within the pond are already heterogeneous. Instead, after finding a hotspot in CH_4 emission at the pond shore, we would like to highlight the need for spatially representative observation and mapping of CH_4 fluxes to understand the variability of pond-CH_4 emissions better.

4.3 Upscaling the CO_2 flux

We upscale the CO_2 emissions for the river terrace of Samoylov, the area where we have access to the high-resolution land-cover classification. We find that not accounting for pond-CO_2 emission leads to an overestimating the polygonal tundra landscape's sink function by 11%. A similar approach by Abnizova et al. (2012) found a potential increase of 35 - 62 % in the estimate of CO_2 emission from the Lena River Delta when including small ponds and lakes into the landscape CO_2 emission. If we follow the upscaling approach by Abnizova et al. (2012) and consider overgrown water as part of the ponds, we even find a CO_2 emission reduction of 19%. Kuhn et al. (2018) also found water bodies in arctic regions to be an important source of carbon, which could outbalance the tundra's sink function in a future climate. In summary, our results demonstrate that open-water CO_2 emissions can substantially influence the carbon balance of the polygonal tundra during the growing season. When looking at the night-time emissions, we find that per gram CO_2-C 0.06 g CH_4-C are emitted from ponds and only 0.02 g CH_4-C from the semi-terrestrial tundra. This finding underlines again, that especially when considering thermokarst ponds, CH_4 emissions are of high interest. Even though mean CH_4 emissions from the semi-terrestrial tundra and open water are of similar magnitude, we expect that the impact of ponds on the carbon balance would be even bigger when accounting for CH_4 due to the locally high emissions.

Our results indicate that future studies aiming to capture a representative landscape flux should pay extra attention to the water bodies in their footprint. The CO_2 flux from ponds has the opposite sign to the tundra. Consequently, ponds should cover about as much area in the footprint as they do in the landscape. In this way, the chances of capturing CH_4 hotspots are also higher, which can then be investigated more closely.

5 Conclusions

We find that thermokarst ponds are a carbon source. At the same time, the surrounding tundra is a carbon sink during the period July – September in agreement with prior studies (Abnizova et al., 2012; Jammet et al., 2017), even if we observe much lower open-water CO_2 fluxes compared to previous work at the same study site (Abnizova et al., 2012). Using our approach to disentangle the EC fluxes from different land cover classes, we gauge that during the measurement period, not accounting for ponds leads to overestimating the landscape CO_2 sink by 11%. We expect lakes to have a similar effect on the budget, though a smaller one, since lakes (a) cover a similar area as ponds in our study site (Abnizova et al., 2012; Muster et al., 2012) (b) are weaker emitters of greenhouse gases than ponds (Holgerson and Raymond, 2016; Wik et al., 2016).

In contrast to the spatially more homogeneous CO_2 emissions, small-scale heterogeneity in CH_4 emissions makes it difficult to find drivers of CH_4 emissions. We cannot pinpoint the drivers behind the high emissions at parts of the coastline, potentially caused by seep ebullition. Thus, we cannot estimate the impact of this heterogeneity on the landscape scale and, therefore, refrain from upscaling CH_4 emissions. Additionally, the open-water fluxes presented in this paper originate from a single merged polygonal pond since the other ponds surrounding the EC tower are too small to extract their fluxes with the footprint method applied here. So, we do not account for spatial variability of CH_4 emissions between ponds, which can be substantial (Rehder et al., 2021; Wik et al., 2016). However, we note that open-water fluxes were of a similar magnitude as the tundra fluxes. Consequently, the main impact of ponds on the landscape CH_4 budget might be through plant-mediated transport and local ebullition.

While being ill-suited for smaller ponds, we want to underline that the EC method is appropriate for observing greenhouse-gas fluxes from ponds with an area as small as 0.024 km^2. The EC method has a higher temporal resolution than the TBL method. It does not disturb the exchange processes like the chamber-flux method, eliminating the wind at the water surface. Especially when combining the EC footprint with a land cover classification, we can distinguish the contribution of different land cover classes well and study the fluxes from ponds.

We conclude that ponds contribute significantly to the landscape carbon budget. Changes in the Arctic hydrology and the concomitant changes in the water-body distribution may impact the overall carbon budget of the Arctic and flip a landscape from being an overall carbon sink to becoming an overall carbon source.

Code and data availability. The data has been published at Pangaea (doi will be added as soon as it becomes available). Code can be requested from the authors.

Appendix A: Additional figures

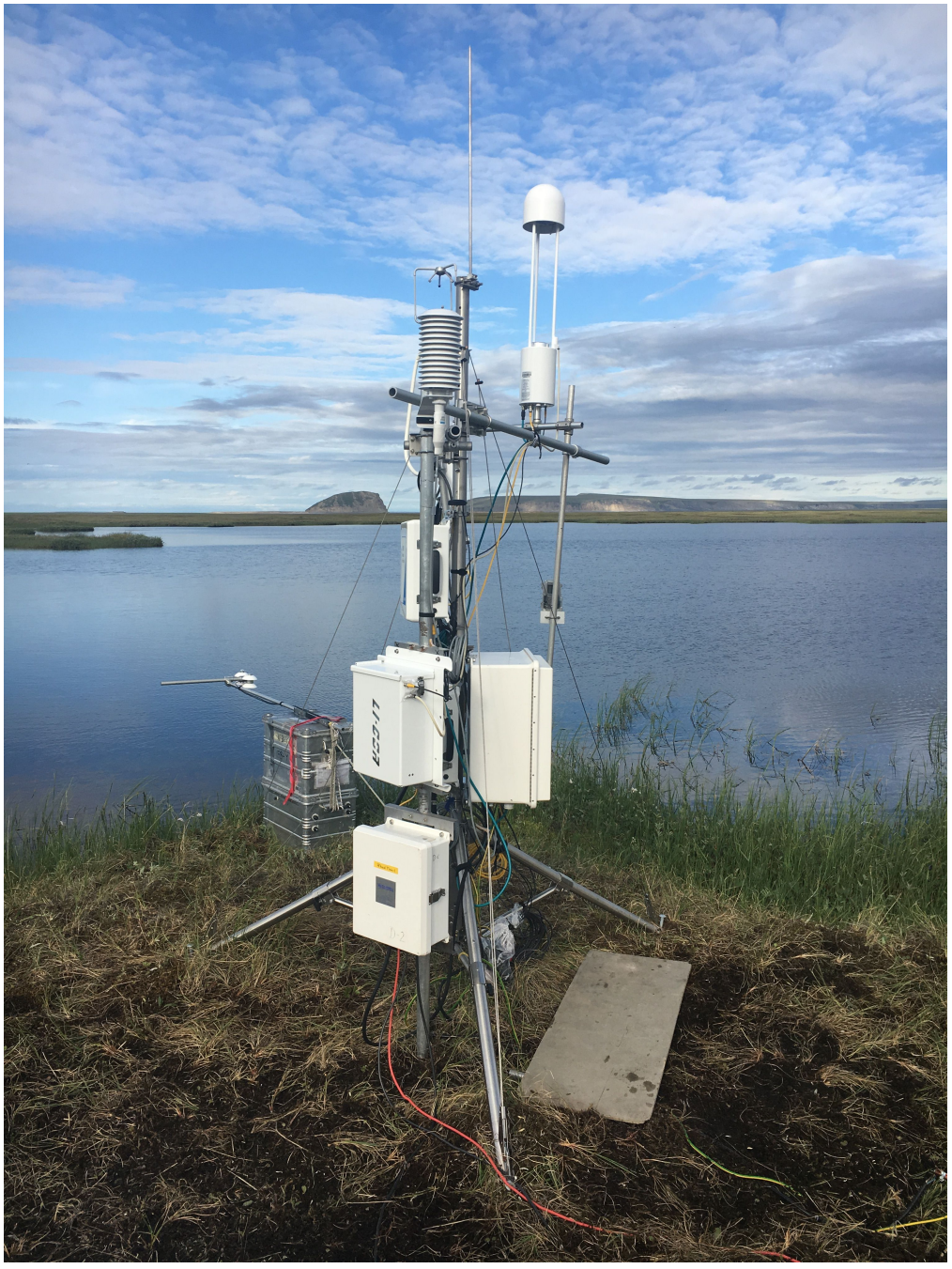

Figure A1. Picture of the eddy covariance tower with the merged polygonal pond in the background. Picture taken on 11 July 2019 by Zoé Rehder.

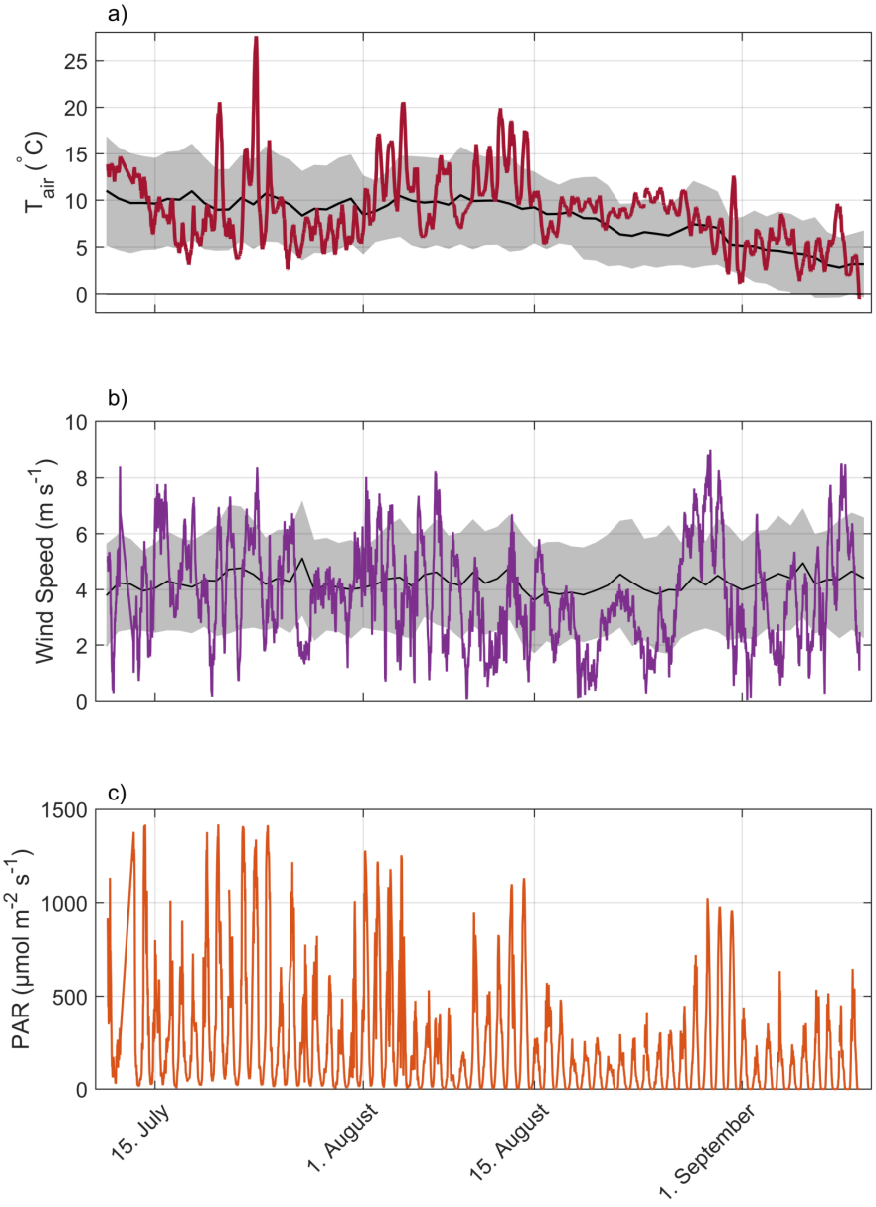

Figure A2. Timeline of observed meteorological conditions during the observation period with air temperature in 2 meters height (a), wind speed in 3 meters height (b) and photosynthetically active radiation (PAR) (c). Mean values and standard deviation of observations during the past 16 years are plotted as black lines and gray areas.

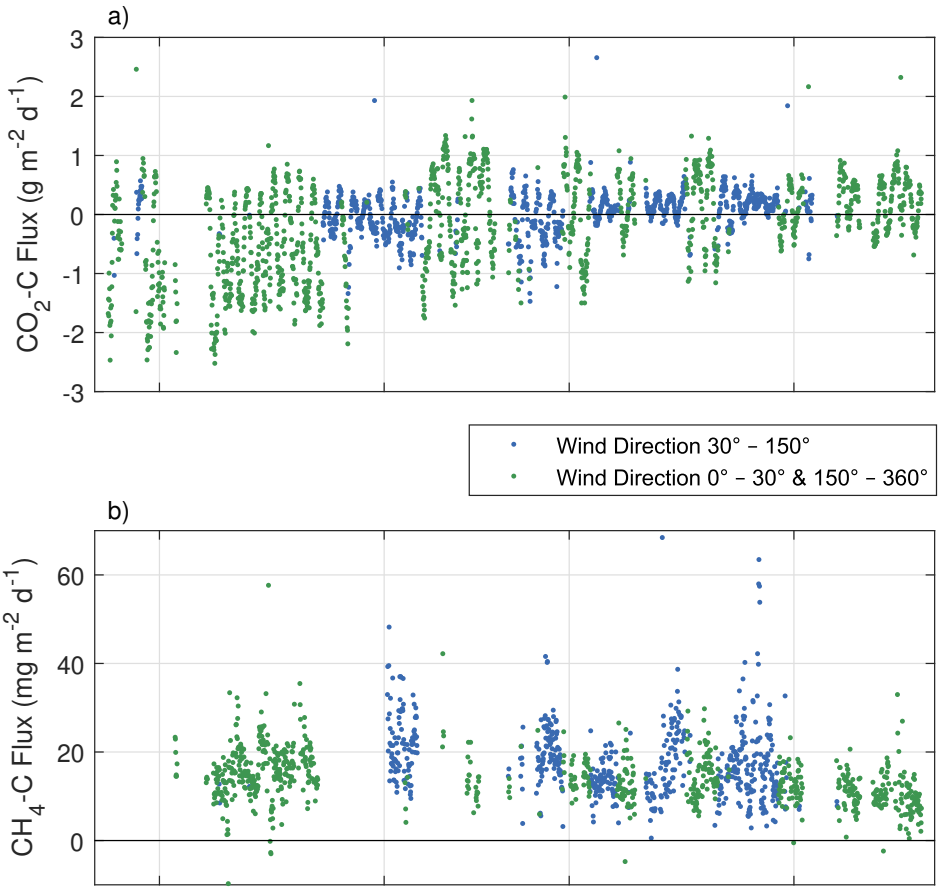

Figure A3. Time series of 30-minute observed CO_2-C flux intervals (a) and CH_4-C flux with a quality flag of 0 or 1. The blue color represents fluxes originating from the wind direction of the lake ($30^\circ - 150^\circ$ wind direction, mostly mixed signals from semi-terrestrial tundra and the lake surface) and the green color represents fluxes originating from all other wind directions.

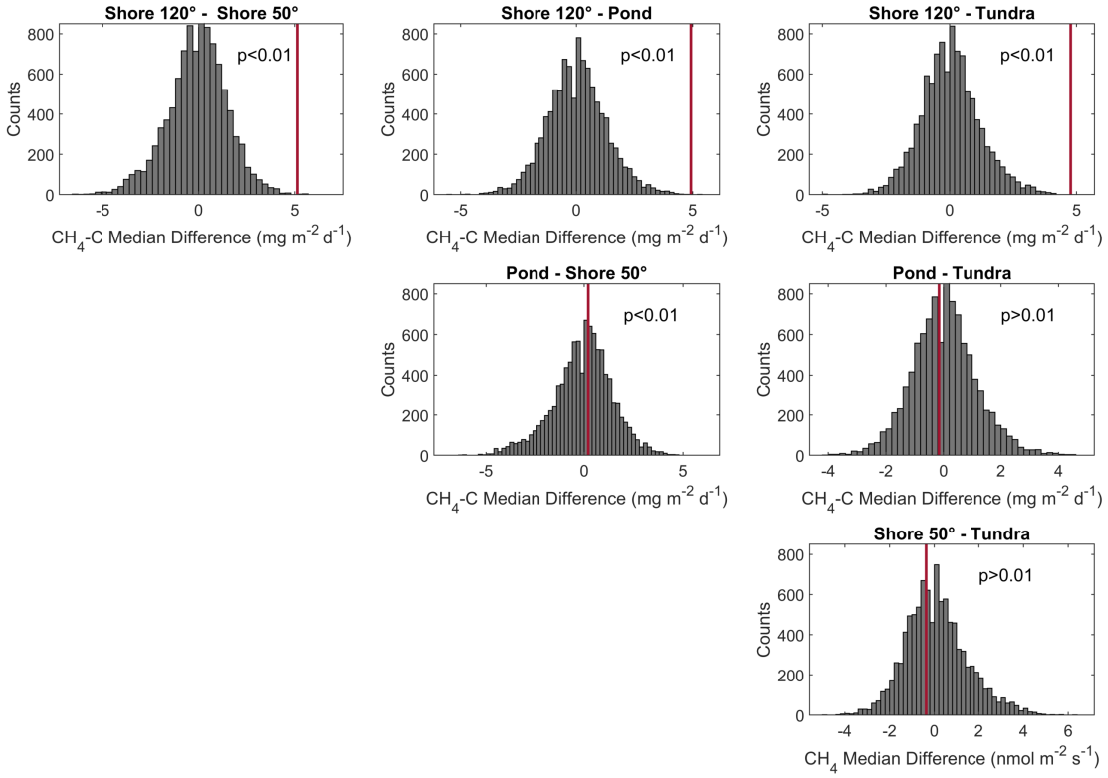

Figure A4. Histogram of permutation tests between the medians of CH_4 emissions from different wind direction classes in figure 6. All medians from flux observations during moderate wind speed conditions. The observed differences in medians between the different wind direction classes are shown in red vertical bars in each plot.

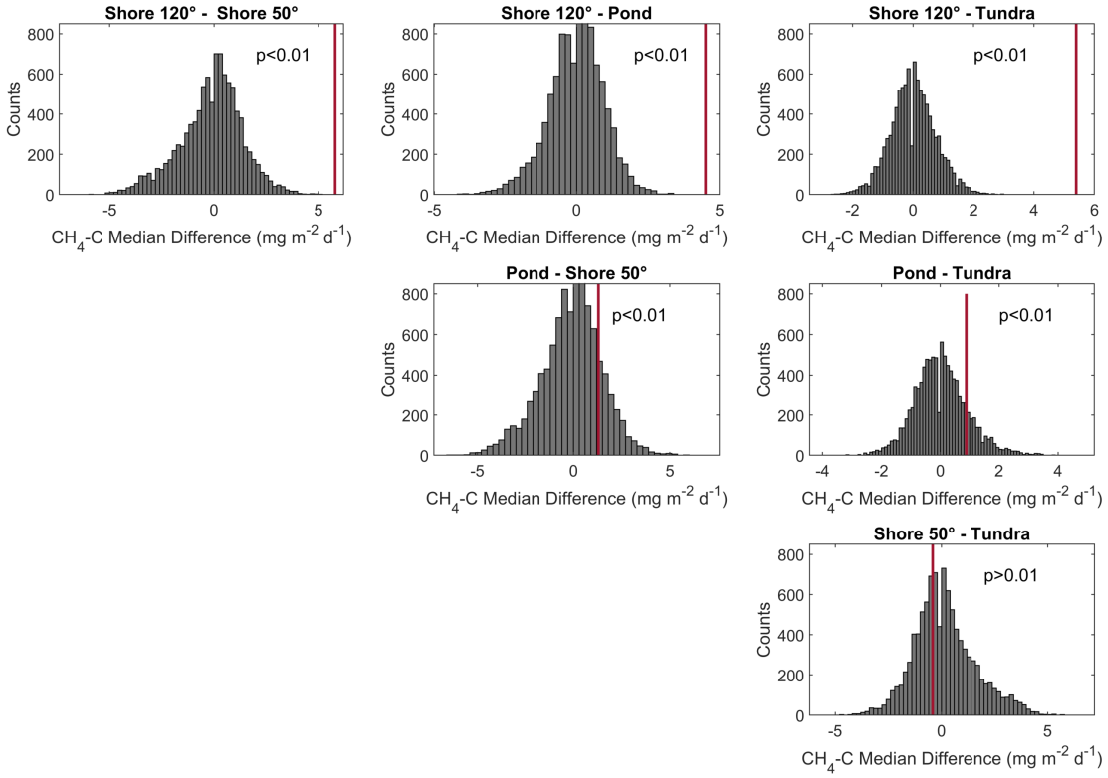

Figure A5. Histogram of permutation tests between the medians of CH_4 emissions from different wind direction classes in figure 6. All medians from flux observations during moderate air temperature conditions. The observed differences in medians between the different wind direction classes are shown in red vertical bars in each plot.

Author contributions. Zoé Rehder and Lars Kutzbach designed the experiments, Zoé Rehder and Lutz Beckebanze carried out the fieldwork. Zoé Rehder, Lutz Beckebanze, and Lars Kutzbach developed the idea for the analysis, and Christian Wille and Lutz Beckebanze prepared the data. The formal analysis and data visualization were performed by Lutz Beckebanze and Zoé Rehder with supervision by David Holl and Lars Kutzbach. Resources (land cover classification) have been provided by Charlotta Mirbach. Lutz Beckebanze and Zoé Rehder prepared the manuscript with contributions from all co-authors.

Competing interests. The authors declare that they have no conflict of interest.

Disclaimer. This study was funded by the Deutsche Forschungsgemeinschaft (DFG, German Research Foundation) under Germany's Excellence Strategy – EXC 2037 'CLICCS - Climate, Climatic Change, and Society' – Project Number: 390683824, contribution to the Center for Earth System Research and Sustainability (CEN) of Universität Hamburg and by the BMBF KoPf project (grant 03F0764B).

Acknowledgements. The authors thank Norman Rüggen for his tireless support before and remotely during the fieldwork, Anna Zaplavnova, Andrei Astapov, and Waldemar Schneider for their equally tireless support in the field, Andrei Astapov and Katya Abramova for additional pictures in the field, Volkmar Assmann and the station crew of Samoylov Island for their logisitical support and Sarah Wiesner, Leonardo Galera, and Tim Eckahardt and for fruitful discussions during the data analysis. Also, the authors thank the reviewers.

References

Abnizova, A., Siemens, J., Langer, M., and Boike, J.: Small ponds with major impact: The relevance of ponds and lakes in permafrost landscapes to carbon dioxide emissions, Global Biogeochemical Cycles, 26, https://doi.org/10.1029/2011gb004237, 2012.

Andresen, C. G. and Lougheed, V. L.: Disappearing Arctic tundra ponds: Fine-scale analysis of surface hydrology in drained thaw lake basins over a 65 year period (1948–2013), Journal of Geophysical Research-Biogeosciences, 120, 466–479, https://doi.org/10.1002/2014jg002778, 2015.

Andresen, C. G., Lara, M. J., Tweedie, C. E., and Lougheed, V. L.: Rising plant-mediated methane emissions from arctic wetlands, Global Change Biology, https://doi.org/10.1111/gcb.13469, 2017.

Bogard, M. J., del Giorgio, P. A., Boutet, L., Chaves, M. C. G., Prairie, Y. T., Merante, A., and Derry, A. M.: Oxic water column methanogenesis as a major component of aquatic CH_4 fluxes, Nature Communications, 5, 5350, https://doi.org/10.1038/ncomms6350, 2014.

Boike, J., Grüber, M., Langer, M., Piel, K., and Scheritz, M.: Orthomosaic of Samoylov Island, Lena Delta, Siberia, https://doi.org/10.1594/PANGAEA.786073, 2012.

Boike, J., Georgi, C., Kirilin, G., Muster, S., Abramova, K., Fedorova, I., Chetverova, A., Grigoriev, M. N., Bornemann, N., and Langer, M.: Temperature, water level and bathymetry of thermokarst lakes in the continuous permafrost zone of northern Siberia - Lena River Delta, Siberia, https://doi.org/10.1594/PANGAEA.846525, 2015a.

Boike, J., Veh, G., Stoof, G., Grüber, M., Langer, M., and Muster, S.: Visible and near-infrared orthomosaic and orthophotos of Samoylov Island, Siberia, summer 2008, with links to data files, https://doi.org/10.1594/PANGAEA.847343, 2015b.

Boike, J., Veh, G., Viitanen, L.-K., Bornemann, N., Stoof, G., and Muster, S.: Visible and near-infrared orthomosaic of Samoylov Island, Siberia, summer 2015 (5.3 GB), https://doi.org/10.1594/PANGAEA.845724, 2015c.

Boike, J., Nitzbon, J., Anders, K., Grigoriev, M. N., Bolshiyanov, D. Y., Langer, M., Lange, S., Bornemann, N., Morgenstern, A., Schreiber, P., Wille, C., Chadburn, S., Gouttevin, I., and Kutzbach, L.: Meteorologic data at station Samoylov (2002-2018, level 2, version 201908), link to archive, PANGAEA, https://doi.org/10.1594/PANGAEA.905232, 2019.

Borrel, G., Jézéquel, D., Biderre-Petit, C., Morel-Desrosiers, N., Morel, J.-P., Peyret, P., Fonty, G., and Lehours, A.-C.: Production and consumption of methane in freshwater lake ecosystems, Research in Microbiology, 162, 832–847, https://doi.org/10.1016/j.resmic.2011.06.004, 2011.

Bouchard, F., Laurion, I., Preskienis, V., Fortier, D., Xu, X., and Whiticar, M. J.: Modern to millennium-old greenhouse gases emitted from ponds and lakes of the Eastern Canadian Arctic (Bylot Island, Nunavut), Biogeosciences, 12, 7279–7298, https://doi.org/10.5194/bg-12-7279-2015, 2015.

Bring, A., Fedorova, I., Dibike, Y., Hinzman, L., Mard, J., Mernild, S. H., Prowse, T., Semenova, O., Stuefer, S. L., and Woo, M. K.: Arctic terrestrial hydrology: A synthesis of processes, regional effects, and research challenges, Journal of Geophysical Research-Biogeosciences, 121, 621–649, https://doi.org/10.1002/2015jg003131, 2016.

Burba, G., Schmidt, A., Scott, R. L., Nakai, T., Kathilankal, J., Fratini, G., Hanson, C., Law, B., Mcdermitt, D. K., Eckles, R., Furtaw, M., and Velgersdyk, M.: Calculating CO_2 and H_2O eddy covariance fluxes from an enclosed gas analyzer using an instantaneous mixing ratio, Global Change Biology, 18, 385–399, https://doi.org/10.1111/j.1365-2486.2011.02536.x, 2012.

Conrad, R.: Contribution of hydrogen to methane production and control of hydrogen concentrations in methanogenic soils and sediments, FEMS Microbiology Ecology, 28, 193–202, https://doi.org/10.1016/S0168-6496(98)00086-5, 1999.

Donis, D., Flury, S., Stöckli, A., Spangenberg, J. E., Vachon, D., and McGinnis, D. F.: Full-scale evaluation of methane production under oxic conditions in a mesotrophic lake, Nature Communications, 8, 1661, https://doi.org/10.1038/s41467-017-01648-4, 2017.

Ducharme-Riel, V., Vachon, D., del Giorgio, P. A., and Prairie, Y. T.: The relative contribution of winter under-ice and summer hypolimnetic CO_2 accumulation to the annual CO_2 emissions from northern lakes, Ecosystems, 18, 547–559, https://doi.org/10.1007/s10021-015-9846-0, 2015.

Edgington, E. and Onghena, P.: Randomization tests, CRC Press, 2007.

Ellis, C. J., Rochefort, L., Gauthier, G., and Pienitz, R.: Paleoecological evidence for transitions between contrasting landforms in a polygon-patterned high arctic wetland, Arctic, Antarctic, and Alpine Research, 40, 624–637, https://doi.org/10.1657/1523-0430(07-059)[ELLIS]2.0.CO;2, 2008.

Encinas Fernández, J., Peeters, F., and Hofmann, H.: On the methane paradox: Transport from shallow water zones rather than in situ methanogenesis is the major source of CH_4 in the open surface water of lakes, Journal of Geophysical Research: Biogeosciences, 121, 2717–2726, https://doi.org/10.1002/2016JG003586, 2016.

Eugster, W., Kling, G., Jonas, T., McFadden, J. P., Wüest, A., MacIntyre, S., and Chapin, F. S.: CO_2 exchange between air and water in an Arctic Alaskan and midlatitude Swiss lake: Importance of convective mixing, Journal of Geophysical Research Atmospheres, 108, https://doi.org/10.1029/2002JD002653, 2003.

Fan, S.-M., Wofsy, S. C., Bakwin, P. S., Jacob, D. J., and Fitzjarrald, D. R.: Atmosphere-biosphere exchange of CO_2 and O_3 in the central Amazon Forest, Journal of Geophysical Research: Atmospheres, 95, 16 851–16 864, https://doi.org/10.1029/JD095iD10p16851, 1990.

Fratini, G., Ibrom, A., Arriga, N., Burba, G., and Papale, D.: Relative humidity effects on water vapour fluxes measured with closed-path eddy-covariance systems with short sampling lines, Agricultural and forest meteorology, 165, 53–63, https://doi.org/10.1016/j.agrformet.2012.05.018, 2012.

Gash, J. H. C. and Culf, A. D.: Applying a linear detrend to eddy correlation data in realtime, Boundary-Layer Meteorology, 79, 301–306, https://doi.org/10.1007/bf00119443, 1996.

Günthel, M., Klawonn, I., Woodhouse, J., Bižić, M., Ionescu, D., Ganzert, L., Kümmel, S., Nijenhuis, I., Zoccarato, L., Grossart, H.-P., and Tang, K. W.: Photosynthesis-driven methane production in oxic lake water as an important contributor to methane emission, Limnology and Oceanography, 65, 2853–2865, https://doi.org/10.1002/lno.11557, 2020.

Hedderich, R. and Whitman, W. B.: Physiology and biochemistry of the methane-producing Archaea, pp. 1050–1079, Springer New York, New York, NY, https://doi.org/10.1007/0-387-30742-7_34, 2006.

Holgerson, M. A. and Raymond, P. A.: Large contribution to inland water CO_2 and CH_4 emissions from very small ponds, Nature Geoscience, 9, 222–226, https://doi.org/10.1038/ngeo2654, 2016.

Ibrom, A., Dellwik, E., Flyvbjerg, H., Jensen, N. O., and Pilegaard, K.: Strong low-pass filtering effects on water vapour flux measurements with closed-path eddy correlation systems, Agricultural and Forest Meteorology, 147, 140 – 156, https://doi.org/10.1016/j.agrformet.2007.07.007, 2007a.

Ibrom, A., Dellwik, E., Larsen, S. E., and Pilegaard, K.: On the use of the Webb-Pearman-Leuning theory for closed-path eddy correlation measurements, Tellus, Series B: Chemical and Physical Meteorology, 59, 937–946, https://doi.org/10.1111/j.1600-0889.2007.00311.x, 2007b.

Iwata, H., Hirata, R., Takahashi, Y., Miyabara, Y., Itoh, M., and Iizuka, K.: Partitioning eddy-covariance methane fluxes from a shallow lake into diffusive and ebullitive fluxes, Boundary-Layer Meteorology, 169, 413–428, https://doi.org/10.1007/s10546-018-0383-1, 2018.

Jammet, M., Dengel, S., Kettner, E., Parmentier, F.-J. W., Wik, M., Crill, P., and Friborg, T.: Year-round CH_2 and CO_2 flux dynamics in two contrasting freshwater ecosystems of the subarctic, Biogeosciences, 14, 5189–5216, https://doi.org/10.5194/bg-14-5189-2017, 2017.

Jansen, J., Thornton, B. F., Jammet, M. M., Wik, M., Cortés, A., Friborg, T., MacIntyre, S., and Crill, P. M.: Climate-sensitive controls on large spring emissions of CH_4 and CO_2 from northern lakes, Journal of Geophysical Research: Biogeosciences, 124, 2379–2399, https://doi.org/10.1029/2019JG005094, 2019.

Jonsson, A., Åberg, J., Lindroth, A., and Jansson, M.: Gas transfer rate and CO_2 flux between an unproductive lake and the atmosphere in northern Sweden, Journal of Geophysical Research: Biogeosciences, 113, 1–13, https://doi.org/10.1029/2008JG000688, 2008.

Kaimal, J. C. and Finnigan, J. J.: Atmospheric boundary layer flows: their structure and measurement, Oxford university press, 1994.

Kartoziia, A.: Assessment of the ice wedge polygon current state by means of UAV imagery analysis (Samoylov Island, the Lena Delta), Remote Sensing, 11, 1627, https://doi.org/10.3390/rs11131627, 2019.

Kling, G. W., Kipphut, G. W., and Miller, M. C.: The flux of CO_2 and CH_4 from lakes and rivers in arctic Alaska, Hydrobiologia, 240, 23–36, https://doi.org/10.1007/BF00013449, 1992.

Knoblauch, C., Spott, O., Evgrafova, S., Kutzbach, L., and Pfeiffer, E. M.: Regulation of methane production, oxidation, and emission by vascular plants and bryophytes in ponds of the northeast Siberian polygonal tundra, Journal of Geophysical Research-Biogeosciences, 120, 2525–2541, https://doi.org/10.1002/2015jg003053, 2015.

Kormann, R. and Meixner, F. X.: An analytical footprint model for non-neutral stratification, Boundary-Layer Meteorology, 99, 207–224, https://doi.org/10.1023/A:1018991015119, 2001.

Kuhn, M., Lundin, E. J., Giesler, R., Johansson, M., and Karlsson, J.: Emissions from thaw ponds largely offset the carbon sink of northern permafrost wetlands, Scientific Reports, 8, 1–7, https://doi.org/10.1038/s41598-018-27770-x, 2018.

LI-COR: EddyPro Version 7.0.6, 2019.

Liss, P. S. and Slater, P. G.: Flux of gases across the Air-Sea interface, Nature, 247, 181–184, https://doi.org/10.1038/247181a0, 1974.

Lundin, E. J., Giesler, R., Persson, A., Thompson, M. S., and Karlsson, J.: Integrating carbon emissions from lakes and streams in a subarctic catchment, Journal of Geophysical Research: Biogeosciences, 118, 1200–1207, https://doi.org/10.1002/jgrg.20092, 2013.

MATLAB: MATLAB Software 2019b, the MathWorks, Natick, MA, USA, 2019.

Mauder, M. and Foken, T.: Documentation and instruction manual of the eddy covariance software package TK2, Univ, Bayreuth, Abt. Mikrometeorol., ISSN, 161489166, 26–42, 2004.

McGuire, A. D., Christensen, T. R., Hayes, D., Heroult, A., Euskirchen, E., Kimball, J. S., Koven, C., Lafleur, P., Miller, P. A., Oechel, W., Peylin, P., Williams, M., and Yi, Y.: An assessment of the carbon balance of Arctic tundra: Comparisons among observations, process models, and atmospheric inversions, Biogeosciences, 9, 3185–3204, https://doi.org/10.5194/bg-9-3185-2012, 2012.

Moncrieff, J., Clement, R., Finnigan, J., and Meyers, T.: Averaging, detrending, and filtering of eddy covariance time series, in: Handbook of micrometeorology, pp. 7–31, Springer, https://doi.org/10.1007/1-4020-2265-4_2, 2004.

Muster, S., Langer, M., Heim, B., Westermann, S., and Boike, J.: Subpixel heterogeneity of ice-wedge polygonal tundra: a multi-scale analysis of land cover and evapotranspiration in the Lena River Delta, Siberia, Tellus B: Chemical and Physical Meteorology, 64, 17 301, https://doi.org/10.3402/tellusb.v64i0.17301, 2012.

Muster, S., Roth, K., Langer, M., Lange, S., Cresto Aleina, F., Bartsch, A., Morgenstern, A., Grosse, G., Jones, B., Sannel, A. B. K., Sjöberg, Y., Günther, F., Andresen, C., Veremeeva, A., Lindgren, P. R., Bouchard, F., Lara, M. J., Fortier, D., Charbonneau, S., Virtanen, T. A., Hugelius, G., Palmtag, J., Siewert, M. B., Riley, W. J., Koven, C. D., and Boike, J.: PeRL: a circum-Arctic Permafrost Region Pond and Lake database, Earth System Science Data, 9, 317–348, https://doi.org/10.5194/essd-9-317-2017, 2017.

Neff, J. C. and Asner, G. P.: Dissolved organic carbon in terrestrial ecosystems: Synthesis and a model, Ecosystems, 4, 29–48, https://doi.org/10.1007/s100210000058, 2001.

Peeters, F., Encinas Fernandez, J., and Hofmann, H.: Sediment fluxes rather than oxic methanogenesis explain diffusive CH_4 emissions from lakes and reservoirs, Scientific Reports, 9, 243, https://doi.org/10.1038/s41598-018-36530-w, 2019.

Ramsar Convention Secretariat: An introduction to the ramsar convention on wetlands (previously The Ramsar Convention Manual), Ramsar Convention Secretariat, Gland, Switzerland, 2016.

Rehder, Z., Zaplavnova, A., and Kutzbach, L.: Identifying drivers behind spatial variability of methane concentrations in East Siberian ponds, Frontiers in Earth Science, 9, 183, https://doi.org/10.3389/feart.2021.617662, 2021.

Repo, M. E., Huttunen, J. T., Naumov, A. V., Chichulin, A. V., Lapshina, E. D., Bleuten, W., and Martikainen, P. J.: Release of CO_2 and CH_4 from small wetland lakes in western Siberia, Tellus, Series B: Chemical and Physical Meteorology, 59, 788–796, https://doi.org/10.1111/j.1600-0889.2007.00301.x, 2007.

Rößger, N., Wille, C., Holl, D., Göckede, M., and Kutzbach, L.: Scaling and balancing carbon dioxide fluxes in a heterogeneous tundra ecosystem of the Lena River Delta, Biogeosciences, 16, 2591–2615, https://doi.org/10.5194/bg-16-2591-2019, 2019a.

Rößger, N., Wille, C., Veh, G., Boike, J., and Kutzbach, L.: Scaling and balancing methane fluxes in a heterogeneous tundra ecosystem of the Lena River Delta, Agricultural and Forest Meteorology, 266-267, 243–255, https://doi.org/10.1016/j.agrformet.2018.06.026, 2019b.

Runkle, B. R., Sachs, T., Wille, C., Pfeiffer, E. M., and Kutzbach, L.: Bulk partitioning the growing season net ecosystem exchange of CO_2 in Siberian tundra reveals the seasonality of it carbon sequestration strength, Biogeosciences, 10, 1337–1349, https://doi.org/10.5194/bg-10-1337-2013, 2013.

Sepulveda-Jauregui, A., Walter Anthony, K. M., Martinez-Cruz, K., Greene, S., and Thalasso, F.: Methane and carbon dioxide emissions from 40 lakes along a north-south latitudinal transect in Alaska, Biogeosciences, 12, 3197–3223, https://doi.org/10.5194/bg-12-3197-2015, 2015.

Sieczko, A. K., Duc, N. T., Schenk, J., Pajala, G., Rudberg, D., Sawakuchi, H. O., and Bastviken, D.: Diel variability of methane emissions from lakes, Proceedings of the National Academy of Sciences, 117, 21 488–21 494, https://doi.org/10.1073/pnas.2006024117, 2020.

Squires, M. M. and Lesack, L. F.: The relation between sediment nutrient content and macrophyte biomass and community structure along a water transparency gradient among lakes of the Mackenzie Delta, Canadian Journal of Fisheries and Aquatic Sciences, 60, 333–343, https://doi.org/10.1139/f03-027, 2003.

Treat, C. C., Marushchak, M. E., Voigt, C., Zhang, Y., Tan, Z., Zhuang, Q., Virtanen, T. A., Räsänen, A., Biasi, C., Hugelius, G., Kaverin, D., Miller, P. A., Stendel, M., Romanovsky, V., Rivkin, F., Martikainen, P. J., and Shurpali, N. J.: Tundra landscape heterogeneity, not interannual variability, controls the decadal regional carbon balance in the Western Russian Arctic, Global Change Biology, 24, 5188–5204, https://doi.org/10.1111/gcb.14421, 2018.

Tuovinen, J.-P., Aurela, M., Hatakka, J., Räsänen, A., Virtanen, T., Mikola, J., Ivakhov, V., Kondratyev, V., and Laurila, T.: Interpreting eddy covariance data from heterogeneous Siberian tundra: land-cover-specific methane fluxes and spatial representativeness, Biogeosciences, 16, 255–274, https://doi.org/10.5194/bg-16-255-2019, 2019.

U.S. Geological Survey, EROS Center: CORONA Satellite Photographs, 1965.

Vickers, D. and Mahrt, L.: Quality control and flux sampling problems for tower and aircraft data, Journal of Atmospheric and Oceanic Technology, 14, 512–526, https://doi.org/10.1175/1520-0426(1997)014<0512:QCAFSP>2.0.CO;2, 1997.

Vonk, J. E., Tank, S. E., Bowden, W. B., Laurion, I., Vincent, W. F., Alekseychik, P., Amyot, M., Billet, M. F., Canário, J., Cory, R. M., Deshpande, B. N., Helbig, M., Jammet, M., Karlsson, J., Larouche, J., Macmillan, G., Rautio, M., Walter Anthony, K. M., and

Wickland, K. P.: Reviews and syntheses: Effects of permafrost thaw on Arctic aquatic ecosystems, Biogeosciences, 12, 7129–7167, https://doi.org/10.5194/bg-12-7129-2015, 2015.

Walter, K. M., Zimov, S. A., Chanton, J. P., Verbyla, D., and Chapin, F. S.: Methane bubbling from Siberian thaw lakes as a positive feedback to climate warming, Nature, 443, 71–75, https://doi.org/10.1038/nature05040, 2006.

Walter Anthony, K. M. and Anthony, P.: Constraining spatial variability of methane ebullition seeps in thermokarst lakes using point process models, Journal of Geophysical Research: Biogeosciences, 118, 1015–1034, https://doi.org/10.1002/jgrg.20087, 2013.

Webb, E. K., Pearman, G. I., and Leuning, R.: Correction of flux measurements for density effects due to heat and water vapour transfer, Quarterly Journal of the Royal Meteorological Society, 106, 85–100, https://doi.org/10.1002/qj.49710644707, 1980.

Wik, M., Varner, R. K., Anthony, K. W., MacIntyre, S., and Bastviken, D.: Climate-sensitive northern lakes and ponds are critical components of methane release, Nature Geoscience, 9, 99–105, https://doi.org/10.1038/ngeo2578, 2016.